Environmental Science Nano

ROYAL SOCIETY OF CHEMISTRY

PAPER

View Article Online
View Journal | View Issue

Check for updates

Cite this: *Environ. Sci.: Nano*, 2026, **13**, 1978

High-content imaging reveals how tuning nanoparticle hydrophobicity impacts interactions between porous silica nanoparticles and plant biosurfaces

Eric Ostovich, [a] Cheng-Hsin Huang, [b] Lissett G. Diaz, [a] Christy L. Haynes [b] and Rebecca Klaper *[a]

Received 5th September 2025,
Accepted 28th January 2026

DOI: 10.1039/d5en00829h

rsc.li/es-nano

Nanoparticle surface chemistry characteristics are key factors that determine their behavior upon interaction with different organisms. In particular, electrostatic interactions between nanoparticles and plant-type organisms have been well-characterized; however, the impact of the degree of hydrophobicity remains largely unexplored. Here, ultraporous mesostructured silica nanoparticles (UMNs) were functionalized with different ratios of chlorotrimethylsilane (TMS) to 2-[methoxy(polyethyleneoxy)$_{9-12}$propyl]trimethoxysilane (PEG) to systematically tune their hydrophobicity, and were subsequently used to interrogate how the degree of hydrophobicity affects nanoparticle interactions at the biointerface of the green alga, *Raphidocelis subcapitata*. Using high-content imaging and phenotypic profiling, the levels of UMN internalization, subcellular trafficking, and their associated phenotypic and physiological impacts were quantified. Increasing the PEG content on the surface of the UMNs, which decreased particle hydrophobicity, was found to significantly enhance levels of internalization, but did not alter translocation within the cells. Colocalization analyses indicated a strong association between UMNs and F-actin filaments after 1–24 hours of exposure, which was independent of PEG content and degree of UMN hydrophobicity, as there was no significant difference between particle types. However, after 48 hours, cells appeared to have incorporated a portion of UMNs into their cell walls while depositing the remainder into vacuolated spaces. Lastly, UMNs had a significant impact on phenotype complexity, with specific metrics including enhanced chlorophyll production and shifts in cell cycle progression; however, no growth inhibition was observed after 72 hours. Overall, using this approach, it was found that tuning the degree of UMN hydrophobicity had a significant impact on the levels of internalization. However, once inside the cells, the degree of hydrophobicity did not have a significant impact on translocation, phenotype, or physiological response as each particle type elicited similar cellular responses.

Environmental significance

Nanoparticle surface chemistry plays an integral role in facilitating interactions with biological surfaces, and understanding these properties is crucial for informing design of sustainable nanomaterials. Selected facets of nanomaterial surface chemistry, like surface charge, have been well-characterized because it is relatively easy to tune the surface charge with ligand choice or control of solution pH; however, the impact of varied nanoparticle hydrophobicity remains largely unstudied. Here, ultraporous mesostructured silica nanoparticles (UMNs) were synthesized with a range of surface hydrophobicities to explore these interactions, and *Raphidocelis subcapitata*, was used as a general *in vitro* model for plant-type cells. This work directly links the degree of nanoparticle hydrophobicity to cellular uptake, where decreases in hydrophobicity were associated with higher levels of internalization, while concentration had little impact on internalization, likely due to saturation of silica uptake pathways even at lower concentrations.

Introduction

Understanding how nanomaterials interact at the interface of biological systems is important for predicting their behavior in the environment and for engineering better nanomaterials in a safer-by-design context.[1] However, there is currently a lack in the breadth of mechanistic insights as to how

[a] *School of Freshwater Sciences, University of Wisconsin-Milwaukee, Milwaukee, WI, USA. E-mail: rklaper@uwm.edu*
[b] *Department of Chemistry, University of Minnesota-Twin Cities, Minneapolis, MN, USA*

nanoparticle surface properties influence processes like adhesion, uptake, and translocation in plant-type cells. This hinders spaces like nano-enabled agriculture where it is necessary to design nanomaterials that are scalable, economical, and carry a minimal environmental footprint,[2] or phytoremediation strategies where understanding these mechanisms could enhance the uptake and removal of contaminants, like PFAS.[3]

Currently, extensive research has been done to understand the critical role of various nanomaterial surface chemistry parameters, like electrostatics, and how they influence interactions at the biointerface of different organisms.[4–9] With plant cells, in particular, there is a well-established relationship between the charge of nanoparticles and their degree of interaction with plant biosurfaces. For example, using model chloroplast membranes and quartz crystal microbalance with dissipation monitoring, Kim *et al.*, 2022 (ref. 8) showed that positively charged carbon nanodots exhibit preferential adsorption to the lipids in the chloroplast membrane compared to neutral and negatively charged carbon nanodots. Moreover, they also proved that the affinity between positively charged carbon nanodots and chloroplast membranes is facilitated, on the cell side, by the abundance of sulfoquinovosyldiacylglycerol, a sulfolipid with a negatively charged head group in the chloroplast membrane.[8] In another study, Jeon *et al.*, 2023 (ref. 9) explored how the surface charge density on carbon dots affected the electrostatic interactions between the cell walls of plants and algae (*Arabidopsis* and *Choleochaete*, respectively) and nanoparticles. This was done by functionalizing positively charged carbon dots using polyethylenimine (PEI) polymers with different molecular weights (0.6k, 10k, and 25k). Their findings indicated that increasing the surface charge density of the positively charged PEI–carbon dots enhanced their interaction with plant and algal cell walls, and that tuning the surface charge density of nanoparticles provides an approach to control nanoparticle binding and translocation.[9]

Some studies have also been done to address how nanoparticle surface hydrophobicity impacts nanoparticle interactions with plant biosurfaces, as well as other organisms.[10–13] For example, coating gold nanoparticles with hydrophobic polymers has been shown to increase interaction with leaf surfaces and enhance uptake past the cell walls in wheat.[10] Conversely, in HUVEC and C17.2 neural progenitor cells, gold nanoparticle surface hydrophobicity did not substantially affect levels of cellular uptake, but did correlate to higher levels of membrane damage.[13] Similarly, in *C. elegans*, quantum dots functionalized with hydrophobic ligands were shown to associate with the cuticle membrane while exhibiting a lack of particle uptake,[12] thus highlighting key differences in hydrophobic nano–bio interactions between plant-type and animal-type eukaryotic cells.

Comparatively, less research has been done to address how tuning the degree of nanoparticle hydrophobicity influences the level of interaction with plant biosurfaces and internalization into the cell. This relationship is not straightforward as nanoparticles need to be sufficiently hydrophilic to remain stable in aqueous environments, but also exhibit enough hydrophobic character to interact with the amphiphilic species that make up the cell wall and membrane. In this context, ultraporous mesostructured silica nanoparticles (UMNs) offer a promising platform for studying these types of interactions in a controlled, mechanistically relevant manner. UMNs are characterized by having large internal volume, high stability in solution, and a porous shell with ultrahigh pore volume, suitable for carrying molecular cargo.[3,14] As such, UMNs have several potential applications such as plant nutrient and agrochemical delivery, oxygen sensing, and environmental pollutant remediation.[3,14–16] Additionally, silica-based nanomaterials, in general, have large relevancy to plants, especially as related to agriculture where they have applications in disease suppression and promoting plant growth.[17,18] Their silica-based surface and high accessible surface area make them biocompatible and highly tunable, thus allowing for easy functionalization to incorporate a range of functional groups, such as those with varying degrees of hydrophobicity or charge; it is also straightforward to incorporate a fluorophore silane into the synthesis to facilitate stable luminescence for microscopic visualization.[3,14]

In this study, UMNs were functionalized with two different ligands, chlorotrimethylsilane (TMS) and 2-[methoxy(polyethyleneoxy)$_{9–12}$propyl] trimethoxysilane (PEG), to control their surface hydrophobicity, where TMS is a hydrophobic ligand and PEG is a hydrophilic ligand. To tune the degree of their hydrophobicity, the UMNs were functionalized with different molar ratios of TMS : PEG, including 1 : 1, 1 : 2, and 1 : 3. Here, the term, hydrophobicity, is used as a general term to describe the balance between the hydrophilic PEG and hydrophobic TMS surface groups on the UMN surface, however, it should be noted that increasing the PEG-silane content enhances the overall hydrophilicity and correspondingly reduces the relative hydrophobicity of the particle surface. Varying the hydrophilic PEG content was chosen instead of the hydrophobic TMS content because increasing the TMS proportion resulted in particle instability and aggregation during synthesis. Therefore, adjusting the content of PEG chain provides a practical way to tune the overall surface characteristics while maintaining particle stability. Additionally, the UMNs were also synthesized with the fluorophore, rhodamine B isothiocyanate (TERITC) fully incorporated within the core silica structure for stable fluorescence visualization. In order to study their level of interaction at the interface of plant biosurfaces, the unicellular green alga, *Raphidocelis subcapitata*, was used as a general *in vitro* model for plant-type cells due to its similarity to mesophyll cells of higher plants including a rigid cellulose-rich cell wall and conserved cellular structures and pathways, as well as its ease of use with high-content fluorescence imaging.[19–21] Further justification for the use of this model can be found in the supplementary information.

Additionally, this study was done in combination with the multiplexed algal cytological imaging assay (MACI),[21] which utilizes high-content imaging to visualize and measure alterations to subcellular structures as well as the translocation of fluorescently labeled compounds or nanoparticles. MACI, which was developed in *R. subcapitata*, is a phenotypic profiling assay that utilizes fluorescence cytochemistry to visualize multiple subcellular structures and automated high-content imaging to acquire hundreds of morphological snapshots.[21] Since MACI also captures 100's of morphological features at single-cell resolution, including area, shape, quantity, fluorescence intensity, granularity, and spatial-based descriptors, it allows for the measurement of subtle changes in phenotype complexity, which can be useful for predicting mechanisms of action and identifying cellular targets in plant-type organisms.[22]

While largely unexplored, the degree of UMN hydrophobicity is expected to alter the level of nano–bio interactions due to the amphiphilic nature of plant biosurfaces. For example, the cell walls are typically rich in hydrophilic polymers and acidic polysaccharides like cellulose microfibrils, hemicelluloses, and pectins, while the plasma membranes contain lipids and certain integral/glycoproteins with both hydrophobic and hydrophilic regions.[9,23] Therefore, the balance of hydrophobic and hydrophilic ligands on the UMN surface could influence processes like nanoparticle uptake, particularly *via* endocytosis, by promoting initial contact with the outer cell surface, as well as the translocation throughout the cells. As a result, this may also have a potential impact on aspects of plant cell physiology like growth and pigment production. Using high-content imaging and MACI to study UMN interactions, we aim to (1) characterize how the degree of surface hydrophobicity of UMNs affects the level of internalization, (2) compare how the tuned hydrophobic interactions differ from that of well-established electrostatic interactions, (3) characterize how UMNs translocate within the cell, and (4) assess the phenotypic and physiological responses in UMN-exposed cells. Overall, by applying this integrated approach, we aim to expand the current understanding of how tuning nanoparticle surface hydrophobicity can generally impact their interactions with plant biosurfaces.

Materials and methods

UMN synthesis and characterization

The TERITC–UMNs were synthesized by a sol–gel method following our previously reported method with some modifications.[3,15] First, since TERITC cannot be directly incorporated into the silica network, it was first combined with (3-aminopropyl)triethoxysilane (APTES) to form TERITC-silane, which was then introduced into the synthesis. TERITC (2.14 mg) was dissolved in 200 proof ethanol (4 mL), and mixed with APTES (8 μL). The mixture was then stirred in the dark for 19 hours to form the TERITC-silane precursor.

To synthesize the TERITC–UMNs, cetyltrimethylammonium bromide (CTAB, 0.1450 g) was dissolved in Milli-Q water (10 mL). *N*,*N*-Dimethylhexadecylamine (DMHA, 150 μL) and decane (116 μL) were then added to the solution, and the mixture was then stirred for 1 hour at 700 rpm and 50 °C. Next, the mixture was sonicated in a sonication bath (Branson 2510) for 1.5 hours to increase micelle formation. Simultaneously, NH_4OH solution (0.256 M, 150 g) was added to an Erlenmeyer flask and stirred at 300 rpm and 50 °C. The micelle solution was transferred into the Erlenmeyer flask containing the NH_4OH solution after sonication. After that, ethanolic tetraethyl orthosilicate (TEOS, 0.88 M, 2.5 mL) and the pre-made TERITC-silane solution (1 mL) was added dropwise to the solution *via* an addition funnel, and the mixture was stirred at 700 rpm and 50 °C for 1 hour. All the following procedures were performed with the mixture covered by aluminum foil to prevent light exposure. PEG (450, 900, or 1350 μL for UMN 1 : 1, 1 : 2, or 1 : 3, respectively) was then added dropwise to the mixture to functionalize the UMN surface, and the mixture was stirred at 700 rpm and 50 °C for 30 minutes. Following that, TMS (68 μL) was added to the solution, and the mixture was stirred at 700 rpm and 50 °C for another 30 minutes. After incorporating all surface modifications, the reaction mixture was aged at 50 °C for 16–18 hours. Solutions were then transferred to a glass bottle and hydrothermally treated at 90 °C for 24 hours.

After the hydrothermal treatment, the TERITC–UMN suspension was vacuum filtered with a Buchner funnel, and the filtrate was transferred to centrifuge tubes. The suspension was then centrifuged (Beckman Coulter Optima L) at 66 000 × *g* under vacuum (4 °C, 35 minutes). After the centrifugation, the supernatant was removed, and the pellet was re-suspended in a NH_4NO_3 solution (6 g L^{-1} in 190 proof ethanol). The suspension was stirred at 700 rpm and refluxed at 50 °C for 1 hour to remove the CTAB through an ion exchange reaction. Next, the suspension was centrifuged again and washed with 190 proof ethanol. The reflux and washing steps were repeated again, followed by a final wash with 200 proof ethanol. Finally, the pellet was re-suspended in 200 proof ethanol and dried *via* rotary evaporator. Dynamic light scattering and zeta-potential measurements of UMN suspensions in algae media (found in SI) were obtained with a Zetasizer Nano ZS Size Analyzer from Malvern Panalytical. Additionally, an Agilent BioTek Synergy H4 hybrid microplate reader was used to characterize the fluorescence intensity across particle type (found in SI), and transmission electron microscopy (TEM) was used to visualize UMN morphology after surface functionalization.

Algal cell culture

A stock culture of *R. subcapitata* was inoculated in Bold's modified freshwater solution (Sigma; B5282) at 1 × 10^5 cells per mL and grown in a 1 L Erlenmeyer flask. Cells were illuminated continuously with a full spectrum T8 light bulb with a photon flux of ~70 μE m^{-2} s^{-1}. The stock culture was mixed with an orbital shaker at 111 rpm. The source of the

algae was from an axenic culture of *Selenastrum capricornutum* (old name for *Raphidocelis subcapitata*) from Carolina Biological (item: 152521).

Exposure setup

Several different UMN exposures were done to assess different phenotypic and physiological endpoints at varying time points, including 1-, 24-, and 72 hours. The 1 hour exposure was done to assess initial degrees of internalization, the 24 hour exposure was done to assess phenotypic impacts, and the 72 hour exposure was done to assess growth inhibition. In the 1- and 24 hour exposure, the algal cells were exposed to varying concentrations (between 0–10 ppm) of each UMN type. For each treatment, 900 μL aliquots of algal stock, in exponential growth, were seeded into individual 1.5 mL microcentrifuge tubes, and 100 μL of a 100 ppm UMN stock (1 : 1, 1 : 2, or 1 : 3) and/or algal media were added to each treatment at the appropriate ratios to make up the final UMN concentrations at a final volume of 1 mL. For the 72 hour exposure, treatments were also made at 1 mL suspensions, however, these exposures were done in 24-well plates as the flatter, spread-out, surface allows for the adequate mixing of cells over the longer period of time. In the 1 hour exposure, cells were also treated with commercially available green fluorescent amine-functionalized polystyrene nanoplastics (PSNPs) (25 nm; DiagPoly™, DCFG-L016) to compare hydrophobic interactions to electrostatic interactions using high-content imaging. Before exposing cells to the UMNs or PSNPs, particles were sonicated for 25 minutes to ensure good dispersion. Each exposure was completed with four replicates.

High-content imaging & MACI assay

For the 1 hour exposure, cells were fixed with glutaraldehyde to halt continued UMN interactions, and incubated overnight at 4 °C to minimize enzymatic degradation and maintain the integrity of the subcellular structures. Furthermore, it should be noted that the fixation process *via* glutaraldehyde, itself, only takes around 30 to 60 min, at which point the cell–particle interactions are locked in place due to the covalent cross-linking of biomolecules, thereby preventing further interaction or internalization.[24] However, keeping the cells at 4 °C overnight allows the cells to gently remove themselves from suspension with the remainder of the fluorescent dyes and fixatives in the solution that have not entered the cells, which can otherwise initially cause the cells to stick to the sides of the tubes when centrifuging rather than forming a neat pellet. This is important as it will contribute to the overall downstream quality of the fluorescent images by greatly reducing the amount of background fluorescence. After incubating reactions, cells were centrifuged at 4000 × *g* for 5 min, washed 2× with 1× phosphate buffered saline (PBS), and resuspended in PBS. Cells were then loaded into glass bottom 384-well plates (Cellvis, P384W-1.5H-N) at a seeding density of ~2 × 10^3 cells per mm^2 for the optimal distribution of cells across the well surface. After loading cells, the well plate was spun gently at 600 RPM for 1 minute to concentrate cells at the bottom of the well. UMN-treated cells were imaged with the CY5 and TRITC fluorescent channels to visualize the chloroplast and UMNs, respectively, while the PSNP-treated cells were imaged with the CY5 and GFP fluorescent channels to visualize the chloroplast and PSNPs, respectively. In an additional 1 hour exposure, UMN-treated cells were also stained with rhodamine phalloidin (Thermo Fisher, T7471) to conduct a colocalization analysis between the UMNs and F-actin, which was imaged with the Texas red fluorescent channel. Cells were stained, fixed with glutaraldehyde, and incubated overnight at 4 °C to minimize enzymatic degradation and maintain the integrity of the subcellular structures. After incubating reactions, cells were centrifuged at 4000 × *g* for 5 min, washed 2× with 1× PBS, resuspended in PBS, and plated into a 384 well plate. For the 24 hour exposure, the MACI assay was carried out using methods described by Ostovich & Klaper, 2023.[21] At the end of the exposure, commercially available fluorescent probes were used to stain nuclei and lipid droplets using NucBlue (Thermo Fisher, R37605) and BODIPY 505/515 (Thermo Fisher, D3921), respectively. Glutaraldehyde was also used to fix the algal cells. After adding reagents, all reactions were incubated overnight, at 4 °C to minimize enzymatic degradation and maintain the integrity of the subcellular structures. After incubating reactions, cells were centrifuged at 4000 × *g* for 5 min, washed 2× with 1× PBS, and resuspended in PBS. Cells from each sample were loaded into a well of a glass bottom 384 well plate at a seeding density of ~2 × 10^3 cells per mm^2. In addition to the usual imaging of added fluorescent dyes, the UMN-incorporated TERITC facilitated distinct visualization of the added nanoparticles under the TRITC fluorescent channel (Fig. 1). For the 72 hour exposure, 25 mL aliquots were taken from each sample and loaded into a well of a glass bottom 384 well plate. After loading cells, the well plate was spun gently at 600 RPM for 1 minute to concentrate cells at the bottom of the well, and then incubated in the dark at room temperature for an additional 30 min to ensure all cells had settled to the bottom. For this exposure, cells were only imaged with the CY5 fluorescence filter to get a cell count measurement. For

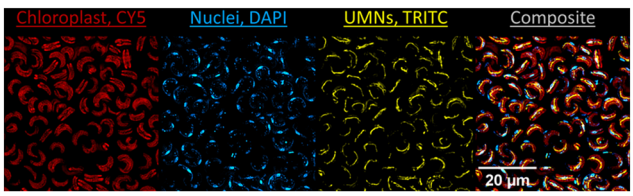

Fig. 1 Fluorescent images of UMN-exposed *R. subcapitata* cells. Representative fluorescence micrographs where each image represents a different fluorescently labeled subcellular compartment visualized, all at the same magnification indicated by the scale bar in the composite image. Lipid droplets (not shown) were also analyzed using the GFP fluorescent channel.

all exposures, images were acquired at 9 sites per well with an ImageXpress Micro XLS high-content screening system with a 60× Plan Fluor 0.85 NA air immersion objective (Molecular Devices, 1-6300-0414). Additionally, to enhance image contrast and resolution, the digital confocal feature was used during image acquisition. Lastly, *z*-stacks were taken at a step size of 0.2 μm for 20 steps.

Bioimage processing & analysis

After images were acquired, CellProfiler[25] and Fiji[26] were used for image processing. Specifically, CellProfiler was used for the pre-processing of images, object segmentation, and morphological feature extraction of individual cells. Morphological features related to the area, shape, quantity, intensity, location, and granularity of each subcellular structure were extracted. To analyze the morphological feature data, as described in Ostovich & Klaper, 2023,[21] the data was aggregated to per-well values and then the data was normalized to the non-treated cell control by computing a *Z*-score. Lastly, R Studio was used to perform an ANOVA across all features for each individual fluorophore to remove any non-informative features with little variance (p-values $>$ 0.05), and the mixOmics package was used for performing partial least squares–discriminant analyses (PLS–DA) to assess changes to phenotype complexity.[27–29] Fiji was used to create 3D-projections from the acquired *z*-stacks. Lastly, CellProfiler was also used to mathematically reconstruct the algal cell wall onto nano-exposed cells for approximating levels of nanoparticle uptake. In order to do this, separate, non-nanoparticle-treated cells were stained with safranin-O (Fig. S4), which binds to cellulose fibers in cell walls.[30,31] Cells were stained at a final concentration of 5 μM, fixed with glutaraldehyde, and incubated overnight at 4 °C to minimize enzymatic degradation and maintain the integrity of the subcellular structures. After incubating reactions, cells were centrifuged at 4000 × *g* for 5 min, washed 2× with 1× PBS, resuspended in PBS, and plated into a 384 well plate. For imaging, the CY5 fluorescence filter was used to visualize the chloroplast while the TRITC fluorescence filter was used to visualize the cell wall. After acquiring images, the critical distance in pixels from the border of the cell wall to the border of the chloroplast was determined using CellProfiler (~4 pixels for this specific microscope and objective) (Fig. S5). Lastly, the cell walls were mathematically reconstructed onto the cells by extending the border of the chloroplast by that same critical distance since the chloroplast is the overall shape of the entire cell. This procedure was also implemented on *z*-stacks for 3D visualization (Movie S1–S3). This procedure was done in place of directly staining nanoparticle-treated cells with safranin-O as PSNPs tend to absorb fluorescent dyes, making fluorescent signals uninterpretable (Fig. S3), and its fluorescent signal also overlaps with that of TERITC within the UMNs. After images were acquired, CellProfiler[25] and Fiji[26] were used for image processing. Specifically, CellProfiler was used for the pre-processing of images, object segmentation, and morphological feature extraction of individual cells. Morphological features related to the area, shape, quantity, intensity, location, and granularity of each subcellular structure were extracted. In order to analyze the morphological feature data, as described in Ostovich & Klaper, 2023,[21] the data was aggregated to per-well values and then the data was normalized to the non-treated cell control by computing a *Z*-score. Lastly, R Studio was used to perform an ANOVA across all features for each reference chemical to remove any non-informative features with little variance (p-values $>$ 0.05), and the mixOmics package was used for performing partial least squares–discriminant analyses (PLS–DA) to assess changes to phenotype complexity.[27–29] Fiji was used to create 3D-projections from the acquired *z*-stacks. Lastly, CellProfiler was also used to mathematically reconstruct the algal cell wall onto nano-exposed cells for approximating levels of nanoparticle uptake. In order to do this, separate, non-nano-treated cells were stained with safranin-O (Fig. S4), which binds to cellulose fibers in cell walls.[30,31] Cells were stained at a final concentration of 5 μm, fixed with glutaraldehyde, and incubated overnight at 4 °C to minimize enzymatic degradation and maintain the integrity of the subcellular structures. After incubating reactions, cells were centrifuged at 4000 × *g* for 5 min, washed 2× with 1× PBS, resuspended in PBS, and plated into a 384 well plate. For imaging, the CY5 fluorescence filter was used to visualize the chloroplast while the TRITC fluorescence filter was used to visualize the cell wall. After acquiring images, the critical distance in pixels from the border of the cell wall to the border of the chloroplast was determined using CellProfiler (~4 pixels for this specific microscope and objective) (Fig. S5). Lastly, the cell walls were mathematically reconstructed onto the cells by extending the border of the chloroplast by that same critical distance since the chloroplast is the overall shape of the entire cell. This procedure was also implemented on *z*-stacks for 3D visualization (Movie S1–S3). It is also important to state that this procedure was done in place of directly staining nano-treated cells with safranin-O as PSNPs tend to absorb fluorescent dyes, making fluorescent signals illegible (Fig. S3), and its fluorescent signal also overlaps with that of TERITC on the UMNs. In order to measure the level of UMN internalization, relative internalization was measured as the integrated intensity (sum of intensity pixels) of nanoparticle fluorescence within each cell.

OECD 201 growth inhibition assay

Growth inhibition after 72 hours was measured to determine if the UMNs elicit a toxicological response from algae. High-content imaging and bioimage processing were used to calculate the number of cells per site. This number was then used to calculate the number of cells per well by converting the pixel area (2160 px × 2160 px) to a spatial area (μm^2), using the pixel-to-μm unit conversion for this particular

microscope and objective (0.1078 μm px^{-1}) and then multiplying that by the area of the entire well (10.89 mm^2). Next, the cellular concentration of each treatment was calculated by dividing the number of cells per well by the volume of liquid dispensed into that well. Lastly, cell concentration values at time zero and at 72 hours were used to calculate % growth inhibition using the designated calculations in the OECD guidelines.[32]

Statistical analysis

Statistical analyses were conducted using R Studio.[27,28] A Shapiro–Wilk test was used to verify normal distribution and a two-way ANOVA was used to compare variance among group means, A Tukey *post hoc* test was also used for multiple comparisons, and significant differences were determined with a 95% confidence interval.

Results/discussion

UMN and *Raphidocelis subcapitata* surface characterizations

TEM imaging shows that UMNs have consistent morphology despite having varied functionalization ratios, with a mesoporous shell and a large internal pore, as expected (Fig. 2d). Additionally, all UMN types appeared to be stable in suspension with no aggregation or settling. The UMN surface functionalizations were achieved *via* silane coupling, forming covalent Si–O–Si linkages between the silane and the silica surface, which can be supported by previous work using ^{29}Si solid-state MAS NMR to characterize similarly functionalized silica nanoparticles.[33] In that study, mesoporous silica nanoparticles were functionalized with PEG and TMS using a similar procedure. The ^{29}Si NMR spectra of PEG-modified nanoparticles showed peaks at −58 ppm and −68 ppm, corresponding to the T2 R–Si$(OSi)_2(OH)$ and T3 R–Si$(OSi)_3$ resonance of PEG bonded to the surface, respectively. The TMS-modified nanoparticles also showed an additional peak at 15 ppm (M1, R_3–Si(OSi)), indicating the presence of bonded trimethyl groups on the nanoparticles. The observation of these peaks confirms that the surface functionalizations are covalently attached to the silica framework through Si–O–Si linkages.

Since each ligand is covalently bonded to the UMNs and TERITC is directly incorporated into the network covalent silica structure, this makes these modifications unlikely to disassociate from the nanoparticles mid-exposure. To validate this, dissolution of all UMNs, based on hydrolysis of the

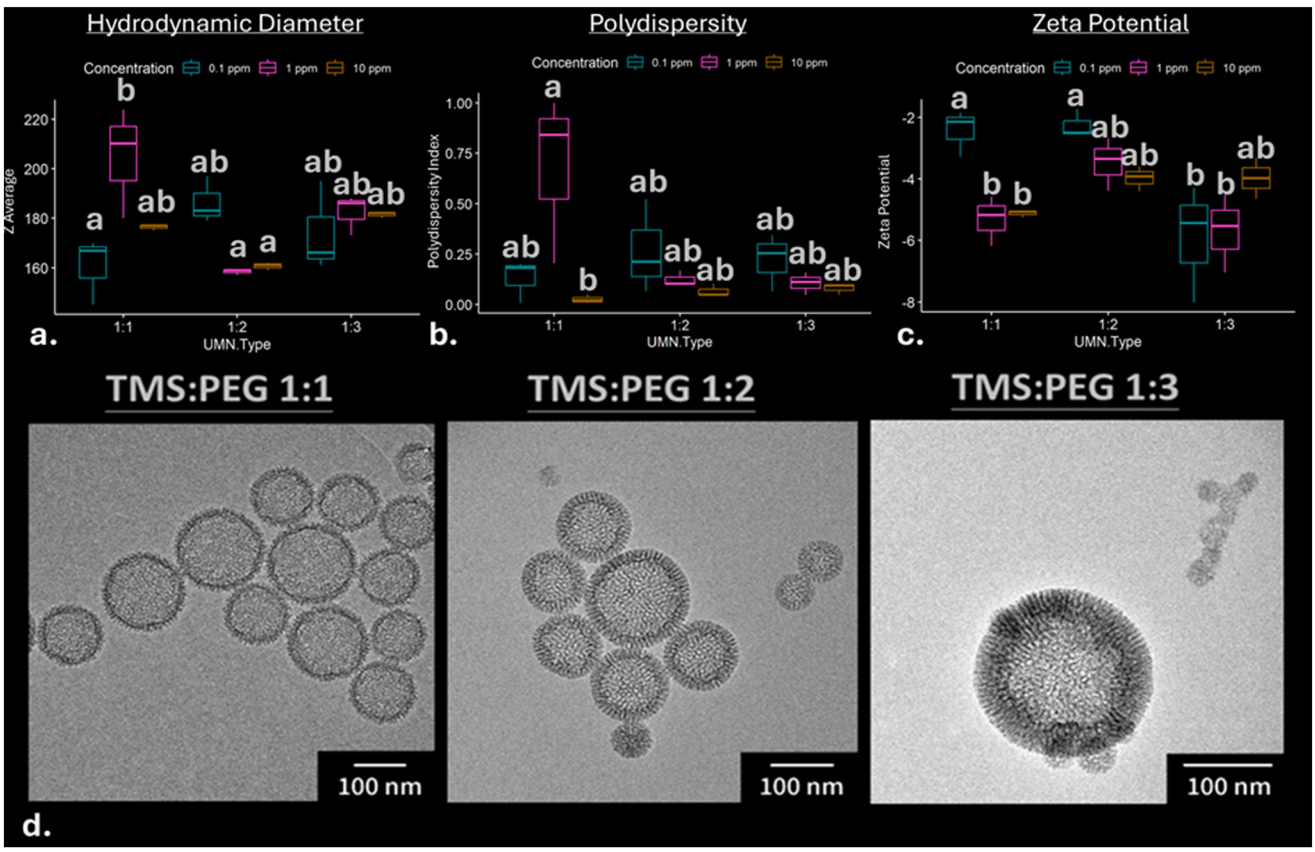

Fig. 2 UMN characterization in algal media. (a) DLS hydrodynamic diameter, (b) polydispersity, and (c) zeta potential. Data was collected in triplicate and significant differences were determined using a two-way ANOVA with a Tukey *post hoc* for multiple comparisons; columns with different letters differ significantly ($p < 0.05$). (d) Transmission electron microscope image of UMNs representing each nanoparticle type with decreasing TMS : PEG to control nanoparticle hydrophobicity. Despite varying functionalization ratios, nanoparticles have consistent morphologies, with a mesoporous structure and a large internal pore.

UMN silica core, was assessed in water over the time period of our algal exposures (~3 days). No significant dissolution of silicic acid from the UMNs was observed within this period (Fig. S1), indicating that the nanoparticles remained stable. Although these measurements were performed in water, the ionic strength of the algal media is relatively low, so similar dissolution behavior under the algal exposure conditions can be expected.

The median hydrodynamic diameter for UMNs suspended in algal media, as measured with dynamic light scattering, was found to be between 170 and 210 nm, depending on the nanoparticle type and concentration (Fig. 2a). Furthermore, UMNs were found to be around neutral charge/slightly negative with a median zeta potential between −2 and −6 mV, depending on nanoparticle type and concentration (Fig. 2c). While adding more PEG chains to the UMNs could in theory reduce the surface charge by decreasing the density of exposed charged silanol groups, this was largely not the case here likely due to the already low zeta potential of the UMNs at the lowest PEG content. The degree of UMN hydrophobicity was also estimated using contact angle measurements (Table S1), however all coated samples exhibited contact angles of ~6°, indicating hydrophilicity beyond the resolution of contact angle measurements for distinguishing between them.

To characterize the relative fluorescence intensities among the nanoparticles with varied TMS : PEG ratios, UMN fluorescence was measured with a plate reader ($\lambda_{ex}/\lambda_{em}$: 560/585 nm) at the same concentration (100 μg mL^{-1}). Fluorescence intensities appeared to significantly decrease with increasing PEG content (Fig. S2). The decrease in fluorescence intensity with increasing PEG content can be a result of changes in both the optical and microenvironmental properties around the fluorescent molecules. Higher PEG content on the nanoparticle surfaces can decrease the local refractive index and increase light scattering,[34] thereby reducing fluorescence brightness. In addition, PEG was introduced to tune surface hydrophilicity and enhance colloidal stability of the nanoparticles in aqueous environments, as PEG chains can form a hydrated layer around the nanoparticle.[35,36] This hydrated PEG shell can also alter the microenvironment around the TERITC molecules, increasing polarity and hydrogen bonding. Previous studies have shown that the fluorescence of common dyes, including rhodamine derivatives, can be quenched in water or highly polar solvents due to O–H vibrations.[37] Together, these effects lead to the observed reduction in fluorescence intensity of nanoparticles with higher PEG content. Therefore, to account for this phenomenon when measuring UMN uptake, each sample fluorescence was normalized to the 1 : 1-TMS–PEG-functionalized UMN samples in corresponding exposures.

Previously, the surface of *R. subcapitata* has also been characterized. In particular, Gonçalves *et al.* 2015 reported *R. subcapitata* as having a largely hydrophilic surface with a water contact angle of around 48.7° and a negative zeta potential of about −48 mV.[38] These physiochemical properties suggest that the cell surface is dominated by negatively charged, hydrophilic functional groups, such as carboxyl and hydroxyl moieties within the cell wall. This agrees with the biochemical characterizations of the *R. subcapitata* cell wall which report it to be rich in cellulose, while also exhibiting acidic polysaccharides and certain glycoproteins, which are predominantly hydrophilic.[19,23]

Degree of UMN hydrophobicity facilitates level of cellular internalization after 1 hour

The UMNs which have interacted with the cells after 1 hour do not appear to have an initial association, or adherence, to the outer cell wall, but rather appear to have internalized. Furthermore, UMNs appeared to have significantly higher levels of internalization with decreasing hydrophobicity, or

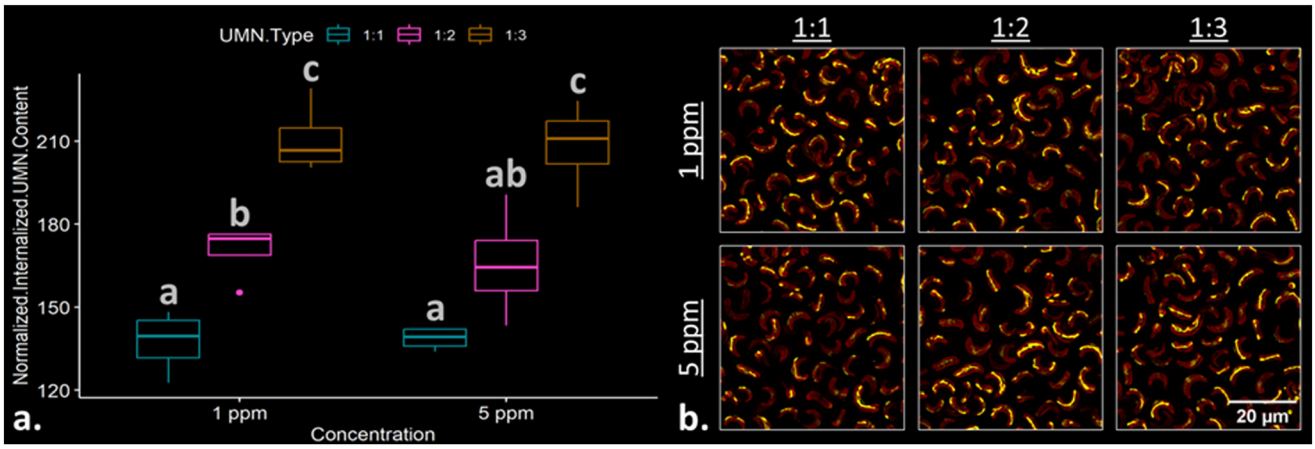

Fig. 3 Internalization of UMNs after 1 hour cell exposure. (a) Normalized fluorescence signal from internalized UMN content across concentration and nanoparticle type. Significant differences were determined using a two-way ANOVA with a Tukey *post hoc* for multiple comparisons; columns with different letters differ significantly ($p < 0.05$). (b) Representative fluorescence micrographs of internalized UMN content across concentration and particle type.

increasing ratios of PEG : TMS, in each exposure concentration tested (Fig. 3a). Exposure concentration did not appear to have any impact on internalization within the same particle exposure. This is likely due to saturation of UMN uptake pathways even at lower concentrations. Silicon is considered a beneficial element to plants and algae because they actively accumulate Si and use it to enhance their ability to withstand biotic and abiotic stresses.[39] Since UMNs are made of silica, it is likely that cells are capable of actively internalizing a certain level of UMNs, and since levels of internalization are consistent despite differing exposure concentrations of the same nanoparticle type, this suggests that the cells have a threshold for how much they will take up. Additionally, the cellular uptake kinetics of nanoparticles, like UMNs, is inherently a saturable process, especially *via* endocytosis.[40] Furthermore, assuming those kinetics have already reached a plateau at the lowest exposure concentrations, increasing the concentration of UMNs would therefore have no additional impact on uptake for the same UMN type. Thus, the enhanced UMN uptake observed in Fig. 3a likely arises from optimizing the density and ratio of hydrophobic and hydrophilic ligands on the UMN surface, thereby enhancing their capacity to internalize larger volumes of UMNs. While the degree of UMN hydrophobicity has an impact on internalization levels, the location of UMNs within the cells does appear to be consistent across particle type and concentration (Fig. 3b), suggesting that the degree of hydrophobicity itself does not impact where the particles translocate within the cells.

Internalization and translocation facilitated by the hydrophobic interactions of UMNs is distinct from the electrostatic interactions of positively charged PSNPs

To get a better understanding of how hydrophobic nanoparticles, like UMNs, interact with plant cell biosurfaces, their internalization patterns were compared to positively charged amine-functionalized PSNPs. In each exposure, cells were exposed to 5 ppm of each nanoparticle type for 1 hour. Then, after acquiring images, cell walls were mathematically reconstructed onto the cells for better visualization and quantification of internalized *vs.* externally bound nanoparticles.

After exposing cells to each nanoparticle type, several differences are apparent. Firstly, PSNPs appear to bind to the exterior of the cell wall to some extent (Fig. 4b), most likely due to the positively charged particle's attraction to the negatively charged cell surface. By comparison, the UMNs that have interacted with the cells after 1 h appear to have fully entered the cells as opposed to associating with the outer surface of the cell (Fig. 4a), likely due to the incompatible electrostatics between the two.

Secondly, when they do internalize, the PSNPs appear to enter and aggregate at random, whereas the UMNs appear to distinctly localize in a specific area of the cell. The area the UMNs initially translocate to after internalizing appears to surround a structural element that runs across the arc of the cell. Since in-depth sub-cellular level fluorescent imaging of *R. subcapitata* is not well-documented in the literature, it was not immediately clear what cellular structure the UMNs could be surrounding or binding to. However, given that the UMNs appear to be localized around a prominent structural element of the cells, we hypothesized that the structure in question could be F-actin filaments, which are important for determining the shape of the cells.[41]

A colocalization analysis was done to test if the particles were associating with F-actin using fluorescence staining with rhodamine phalloidin. Since phalloidin exhibits high specificity for actin filaments, binding to the interface between actin subunits rather than to general hydrophobic surfaces,[42] this dye is ideal for colocalization analysis. Cells were exposed to UMNs for 1 hour, and then stained with rhodamine phalloidin to visualize F-actin filaments. Non-UMN-treated control cells, only stained with rhodamine phalloidin, were done as a reference to validate the binding of rhodamine phalloidin to F-actin, rather than potential association to the UMNs themselves (Fig. S10). After acquiring images, CellProfiler was used to conduct the colocalization measurements. Specifically, a Mander's correlation coefficient[43] with a Costes method of thresholding was used to measure the ratio of UMN pixels that colocalize with actin pixels, but specifically in the context of UMN pixels that are associated with each individual cell, or region of interest (*i.e.* UMN image pixels that are within the region of individual cells as opposed to outside individual cells). This ensured that only the colocalization of foreground signal was being measured, as opposed to any background signal. After conducting this analysis, it was clear that the UMN signal does in fact bear an almost identical location and structure to F-actin filaments, where they appear to be structural elements that run across the arc of the cell (Fig. 5a). Additionally, when merging the two fluorescent signals, there is a nearly perfect overlap between UMN and F-actin in the cells. The Manders correlation coefficient was calculated at a mean of 89%, 89%, and 86% colocalization for 1 : 1, 1 : 2, and 1 : 3 UMNs,

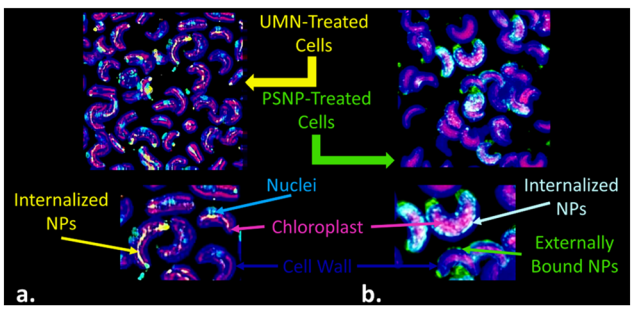

Fig. 4 Hydrophobic interactions *vs.* electrostatic interactions visualized through high-content fluorescent imaging. (a) Algal cells exposed to 5 ppm of 1 : 3 UMNs, representing hydrophobic interactions. (b) Algal cells exposed to amine-functionalized PSNPs, representing electrostatic interactions.

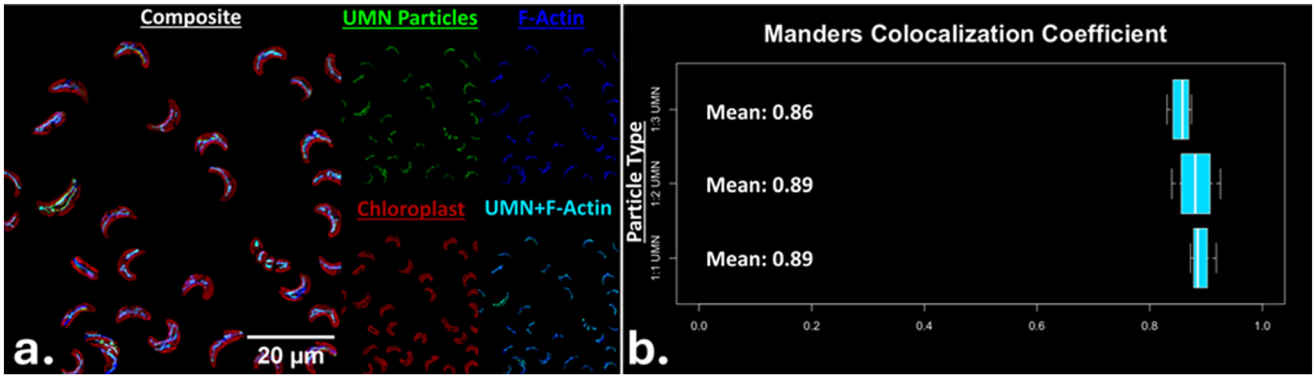

Fig. 5 Colocalization between UMNs and F-actin filaments. (a) Representative images of fluorescently labeled components. In this case, the UMNs were made to look green, and the F-actin was made to look blue for better visual discernment in the composite image. (b) Boxplots representing Manders colocalization coefficient measurements between UMN & F-actin fluorescent signals across nanoparticle type at 10 ppm; no significant differences were observed.

respectively, in which there was no statistical difference between colocalization across nanoparticle type. This indicates a high degree of spatial overlap of fluorescent signals and close proximity between the two structures, and, in turn, suggests a nonrandom interaction between the UMNs and F-actin (Fig. 5b).[44] Currently, there is no obvious reason as to why UMNs would be in close proximity to F-actin in *R. subcapitata*. Unlike other types of phytoplankton, namely diatoms, which have frustules made of silica, *R. subcapitata* does not have a silica-based cell wall, nor does it have any subcellular structures primarily composed of silica. Additionally, while there is no documentation of UMNs, or other silica-based nanoparticles, directly binding to the F-actin filaments of plant and algal cells in the literature, F-actin is documented as playing an important role in many cellular processes in plant cells, which may explain the close initial proximity of the two. For example, in *Arabidopsis* cells, F-actin is involved in clathrin-mediated endocytosis (CME),[45] where F-actin is essential for the invagination and scission of vesicles from the membrane. Additionally, F-actin has been documented in plant and algal cells as being highly involved in cytoplasmic streaming,[41] where it acts as a track for myosin motors to transport vesicles all over the cell. If the UMNs were internalized through CME, which has been reported for green algae with other nanoparticle types,[46] and the subsequent UMN-containing vesicles were being transported throughout the cell, that could explain why there is such close proximity between those two fluorescent signals after a short period of exposure.

To study how UMNs translocate in the cell after longer periods of time, UMN-treated cells were loaded into 384 well plates after 24 hours of exposure, and then kept in the well plate for another 24 hours. Cells were subjected to live imaging, without the use of glutaraldehyde fixation, to allow for UMNs to freely translocate throughout the cell. After 24 hours of exposure, UMNs still appeared to be localized around the F-actin (Fig. 6a), however, after 48 hours, the UMNs appear to have translocated throughout the cells (Fig. 6b). Specifically, a portion of the UMNs appear to have been deposited into the cell wall, while the remaining majority appears to have accumulated largely at the apices of the cells in what looks like terminal vacuolated spaces, similar in location to that of *Closterium moniliferum*.[47] Plant cells are known to incorporate Si and Si-based nanoparticles into their cell walls to fortify it, improve its mechanical properties and regeneration, and increase protection against plant pathogens.[17,18,48] Therefore, in this case, UMN deposition into the cell wall makes sense, especially after a longer period. As opposed to having one central vacuole like higher plant cells, *R. subcapitata* can have many smaller vacuoles across the cell.[49,50] Several of the cells after 48 hours appear to have small bright spots, indicating UMN accumulation in those areas, across the cells in addition to the vacuolated spaces at the cell apices (Fig. 6b). In green algae, like *R. subcapitata*, these vacuoles are

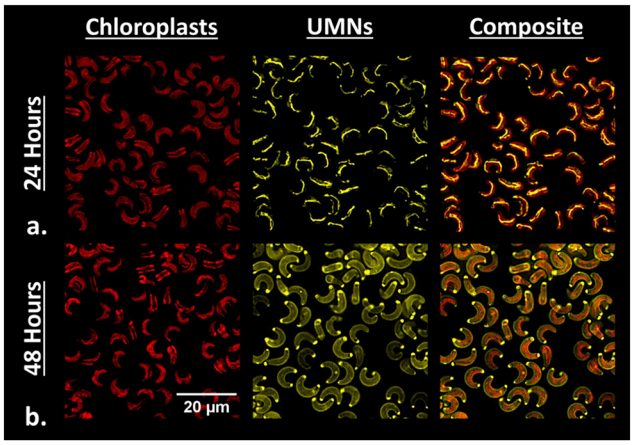

Fig. 6 Translocation of UMN in cells between (a) 24 and (b) 48 hours post exposure. Here the cells were imaged live without the use of glutaraldehyde fixation to allow for UMNs to translocate over a longer period of time.

dynamic organelles with several functions, including storage and detoxification,[51] similar to that of higher plant cells. Therefore, it is likely that excess UMN content would accumulate in those areas of the cell. Based on these results, it would appear that the interactions of UMNs with plant biosurfaces are potentially initiated through CME, and at which point are then streamed throughout the cells along the axis of the F-actin filaments between 1 and 24 hours after initiation of exposure (Fig. 5a and 6a). Then after 48 hours, cells appear to deposit a portion of UMNs into their cell walls and store the remainder in vacuolated spaces (Fig. 6b).

MACI assay suggests that UMNs elicit a significant impact to cell phenotype complexity

After exposing cells to UMNs for 24 hours, they were stained and imaged using the protocol as described by Ostovich & Klaper, 2023.[21] A CellProfiler pipeline was used to extract quantitative data from high-content image data. From these data, over 450 unique, unbiased, morphological features related to area, shape, quantity, intensity, location, and granularity of each subcellular structure were extracted. Phenotypic fingerprints of UMN-treated cells were then generated from these features, and

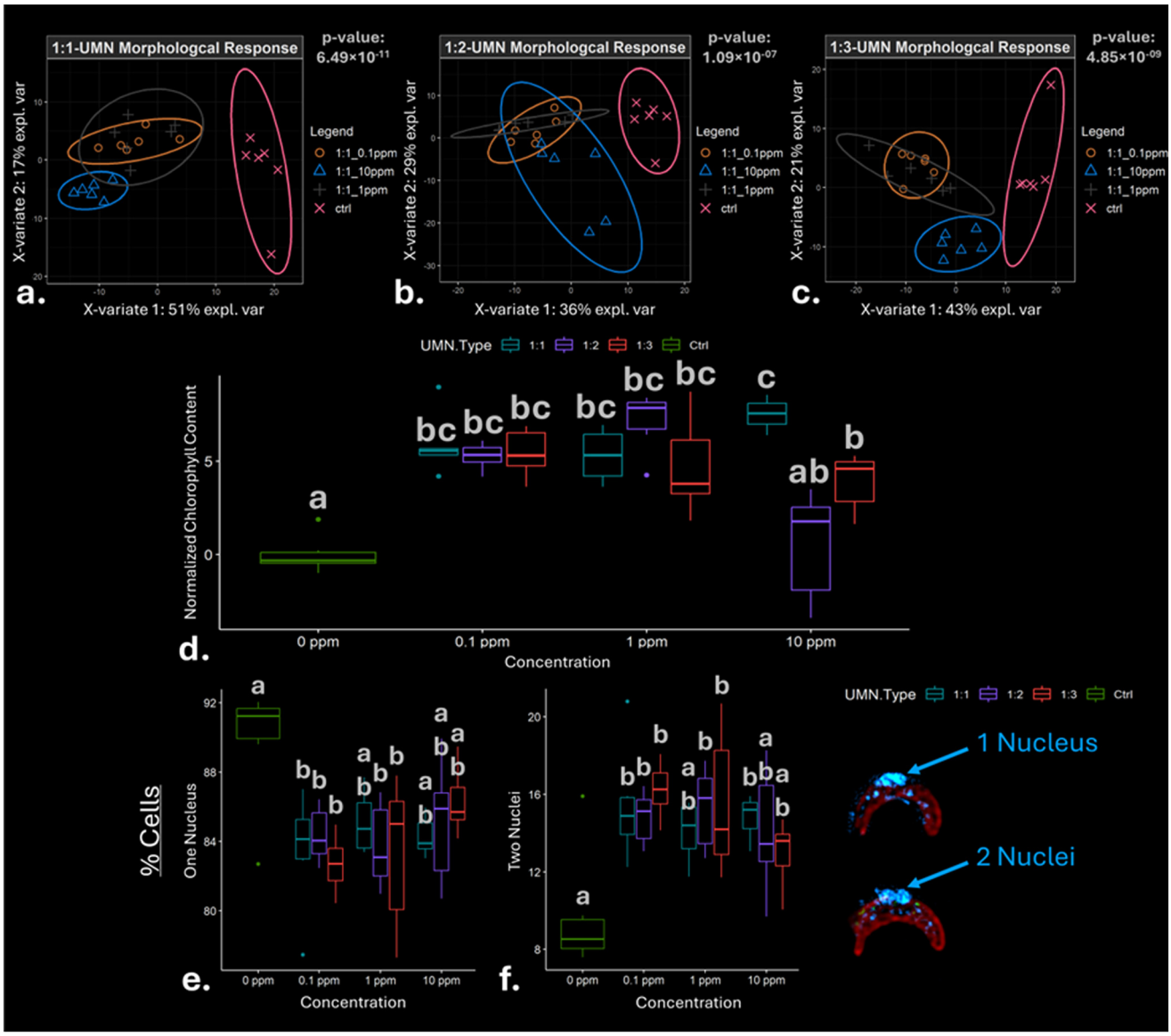

Fig. 7 Phenotypic responses across algal cells after 24 hour-exposure to UMNs with varied hydrophobicity. (a–c) PLS–DA response plots graphically describe changes in complex morphological feature data across UMN concentration and surface chemistry; ellipses represent 95% confidence intervals and *p*-values represent one-way ANOVA statistics across the 1st latent variable between response groups in each plot. (d) Relative chlorophyll content in UMN-exposed algae after 24 hours. (e and f) Percentage of cells with 1 or 2 nuclei, respectively, after 24 hours of UMN exposure. In boxplots, significant differences were determined using a two-way ANOVA with a Tukey *post hoc* for multiple comparisons; columns with different letters differ significantly ($p < 0.05$).

significant changes to phenotype complexity were determined with a partial least squares with discriminant analysis (PLS–DA), a supervised machine learning algorithm that projects multidimensional data onto 2D planes in order to predict responses between groups. PLS–DA plots were created for each nanoparticle type with increasing concentration (Fig. 7a–c). In each plot, there was a significant collective separation between response groups, indicating that UMNs do elicit a significant, and measurable, change to phenotype complexity, and undergo key interactions with subcellular compartments. Interestingly, while each UMN treatment was significantly separated from respective non-treated cell controls, groups representing different concentrations for each nanoparticle type were not and overlapped with one another, thereby indicating that UMN concentration in this range has little impact on phenotype complexity. This may be explained by the levels of UMN uptake after 24 hours (Fig. S10). While the relative uptake levels after 24 hours were greater when compared to the uptake levels after 1 hour (Fig. 3a), they exhibited a similar trend in which the uptake levels were facilitated more by the degree of hydrophobicity than by concentration.

While the majority of the extracted morphological features represent abstract, unbiased descriptors of the cell state, several of the features also have interpretable biological meanings, such as the integrated intensity of the chloroplast and the number of nuclei per cell.[21,22] The integrated intensity associated with the chloroplast has a direct correlation to the relative abundance of chlorophyll in each cell.[52,53] After 24 hours of exposure, UMN-treated cells had mostly produced significantly more chlorophyll content compared to non-treated cell controls across particle type and concentration (Fig. 7d), which recapitulates similar effects in higher land plants exposed to Si-based nanoparticles. For example, wheat plants treated with silica nanoparticles were reported as having significantly higher levels of chlorophyll compared to non-treated plants.[54] The number of nuclei per cell, in which this organism can have up to 8 nuclei at once,[55] has relevance to the cell cycle.[21,55] After 24 hours of exposure, UMN-treated cells had a significantly lower percentage of cells with a single nucleus (Fig. 7e), and a significantly higher percentage of binucleated cells (Fig. 7f) compared to non-treated controls, thus indicating that the UMNs have an impact on cell cycle. Typically, an impact to cell cycle progression, either before or after the first nuclear division, is commonly associated with instances of cell cycle disruption/arrest.[22,56] However, in this case, the concentration of cells in UMN treatments were mostly higher than that of the non-treated controls (Fig. S11), thus indicating more of a stimulatory response to UMN exposure after 24 hours, rather than an inhibitory one. This also bears resembles to higher plants in which exposure to silica-based nanoparticles have been reported to increase growth and yield in various crops.[18]

UMN exposure does not elicit an inhibitory response to cells over a longer period of growth

To further study the physiological impacts of UMN exposure, a growth inhibition assay was conducted following OECD 201 guidelines.[32] Cells were exposed to UMNs over a period of 72 hours, and cell count measurements were taken before and after the exposure duration to calculate the % growth inhibition.[32] Interestingly, % growth inhibition calculations for UMN-treated cells yielded negative results compared to the non-treated cell control (Fig. 8). This indicates that not only do the UMNs lack an inhibitory response across nanoparticle type and concentration after longer periods of growth, but rather that they elicit more of a stimulatory response as recapitulated by the MACI assay results (Fig. 7). Ultimately, the UMNs appear to be relatively benign, lacking a concerning toxicological response.

Conclusion

In this study, UMNs were functionalized with hydrophobic and hydrophilic ligands at different ratios in order to tune the degree of nanoparticle hydrophobicity. High-content imaging revealed that tuning the degree of hydrophobicity of these porous silica nanoparticles does have a measurable and significant impact on algal cell internalization, while lacking an impact on cellular translocation, physiology, and change in phenotypic complexity once inside the cell. These results parallel observations in higher plant systems, where hydrophobic coatings have been shown to enhance nanoparticle uptake, but do not significantly alter their transport and distribution among plant components when compared to nanoparticles with hydrophilic coatings.[10]

The results of this study indicated that decreasing the degree of nanoparticle hydrophobicity was found to facilitate higher levels of UMN internalization in *R. subcapitata*, while particle concentration had little effect, suggesting a

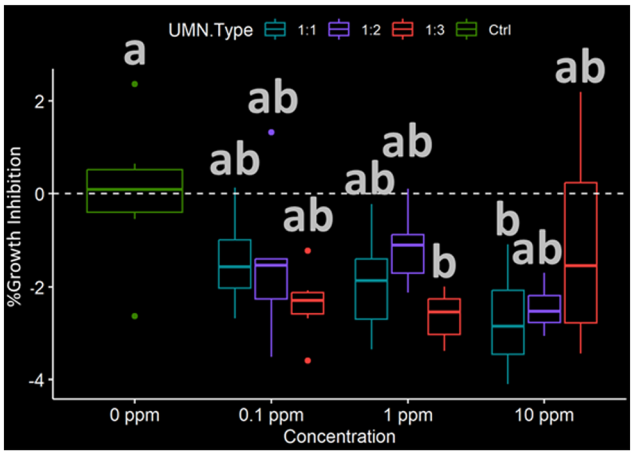

Fig. 8 % Growth inhibition of UMN-exposed cells after 72 hours of exposure. Significant differences were determined using a two-way ANOVA with a Tukey *post hoc* for multiple comparisons; columns with different letters differ significantly ($p < 0.05$).

saturation phenomenon for the uptake of these silica-based nanoparticles even at the lowest doses used. The localization patterns, coupled with F-actin colocalization analyses, suggest that UMN uptake may be initiated *via* clathrin-mediated endocytosis and subsequently trafficked along the actin filaments before being deposited into the cell wall or sequestered into vacuolated spaces. This interaction was distinct from the electrostatic interaction of the positively charged amine-functionalized PSNSs, which predominantly associated with the exterior of the cell wall or internalized and aggregated at random, highlighting the fundamental differences between hydrophobic and electrostatic nano–bio interactions in plant-type systems.

Phenotypic profiling, *via* the MACI assay, revealed significant changes to phenotype complexity and physiology, including enhanced nuclear division patterns and increased chlorophyll content, consistent with previous reports of silicon-based nanoparticles promoting photosynthetic capacity and growth in plants. Furthermore, despite increased levels of internalization with decreasing hydrophobicity, UMN exposure across the board did not induce growth inhibition after 72 hours. Instead, a mild stimulatory effect was observed, indicating a slightly beneficial, or at least benign, physiological impact. Interestingly, in each plot representing an aspect of biometric data (Fig. 7d–f, 8 and S12), the degree of UMN hydrophobicity also seemed to generally have little effect on these physiological readouts in addition to a lack of a dose response. Here, response groups appeared to be separated into a binary of exposed and non-exposed. This would suggest that, while the degree of hydrophobicity facilitates the level of nanoparticle interaction/particle internalization, the physiological impact experienced by the cells is likely more due to the beneficial silica core composition of the nanoparticles rather than their surface functionalization. However, this is not always the case when it comes to nanoparticle impacts. For example, Niemuth *et al.* 2021 reported a ligand-dependent toxicity for hydrophobic quantum dots with cadmium selenide cores when exposed to *C. elgans*.[12]

While *R. subcapitata* serves as a general *in vitro* model to study the interactions between UMNs and plant biosurfaces in this study, extrapolation to whole organism higher plants should certainly be made cautiously. The relationship between the degree of UMN hydrophobicity and cellular uptake observed in this study is likely qualitatively predictive of trends in the cells of higher plant systems due to the general similarities in cell wall compositions. For example, in a study regarding the influence of carbon dot charge on the interactions with cell walls, Jeon *et al.* 2023 found similar trends of adsorption between native extracted cell walls of Arabidopsis and the green algae, Choleochaete.[9] However, quantitative differences in uptake efficiencies and transport are expected due to the complexity of plant tissue when compared to single cell-cultures. In particular, while the mesophyll cells of higher plants are similar to green algal cells like *R. subcapitata*, they often have a waxy cuticle layer as an added non-wettable protection that algal cells lack. Therefore, in order to extrapolate results, an assumption that the UMNs are past the cuticle layer should be made, which could be a reasonable assumption in the context of agricultural practices given that commercial agrochemical products are often formulated with surfactants to penetrate this layer.[57] Beyond intrinsic organismal differences, environmental context and exposure route will further influence the relative uptake of UMNs in in higher plants. For example, in a scenario where UMNs are applied to plant leaves *via* foliar application, the resulting relative levels of uptake would likely be similar to the trends observed in this study. However, in a scenario in which the UMNs are exposed to higher plants *via* soil application, the resulting relative levels of uptake would not be as straight forward due to the complexity of soil as a medium in comparison to an aqueous solution. Therefore, in the context of environmental remediation, such as the phytoremediation of PFAS, higher plant studies would certainly be necessary to make better predictions of uptake and removal in the environment. Although, given the results of this study, there may also be an application for using a type of UMN–algae water treatment for the phytoremediation PFAS contaminated water.

Collectively, these findings extend our understanding of how the degree of nanoparticle hydrophobicity influences nano–bio interactions in plant-type organisms, and that tuning the degree of particle hydrophobicity could potentially be an effective method for enhancing the uptake and delivery of UMNs in plant systems. However, it should also be acknowledged that while these results suggest a correlation between increasing PEG content and increased algal uptake, this effect may not be fully due to the changes in hydrophobicity, but rather a combined effect of multiple factors including surface functional group density and ligand orientation. Therefore, in the future, more studies should be done to experimentally distinguish the individual contributions of each factor. Beyond their mechanistic relevance, these results demonstrate the efficacy of UMNs as a model nanomaterial platform as their tunable surface and biocompatibility make them suitable for probing fundamental interaction principals and informing safer-by-design strategies for agricultural and environmental remediation nanotechnologies. Lastly, the combination of high-content imaging and MACI employed here provides a powerful approach for dissecting nano–bio interactions at the resolution of single cells, thus enabling nuanced comparisons across different nanoparticle surface chemistries.

Conflicts of interest

There are no conflicts of interest to declare from authors.

Data availability

Data supporting this article has been included in the supplementary information (SI), including UMN

characterization data, 3D movies, and supporting cellular phenotypic data.

Supplementary information: UMN characterization data, 3D movies, and supporting cellular phenotypic data. See DOI: https://doi.org/10.1039/d5en00829h.

Acknowledgements

This work was supported by the National Science Foundation under Grant No. CHE-2001611, the NSF Center for Sustainable Nanotechnology. The CSN is part of the Centers for Chemical Innovation Program. The TEM imaging in this study was carried out in the Characterization Facility, University of Minnesota, which receives partial support from the National Science Foundation through the MRSEC program (award number DMR-2011401) and the NNCI (Award Number ECCS-2025124) programs.

References

1 V. Di Battista, K. R. Sanchez-Lievanos, N. Jeliazkova, F. Murphy, G. Tsiliki, A. Zabeo, A. Gajewicz-Skretna, A. Mikołajczyk, D. Hristozov, V. Stone, O. Schmid, N. Hunt, A. G. Oomen and W. Wohlleben, Similarity of multicomponent nanomaterials in a safer-by-design context: the case of core–shell quantum dots, *Environ. Sci.: Nano*, 2024, **11**(3), 924–941.

2 M. Kah, R. S. Kookana, A. Gogos and T. D. Bucheli, A critical evaluation of nanopesticides and and nanofertilizers againts their conventional analogues, *Nat. Nanotechnol.*, 2018, **13**, 677–684.

3 C. H. Huang, R. Lewis, S. Thomas, Z. Tang, J. Jones, S. Nason, N. Zuverza-Mena, Z. A. Piskulich, T. L. O'Keefe, B. Tuga, A. Paredes-Beaulieu, V. Vasiliou, Q. Cui, J. J. Dalluge, J. C. White and C. L. Haynes, Designing Ultraporous Mesostructured Silica Nanoparticles for the Remediation of Per- and Polyfluoroalkyl Substances, *ACS Nano*, 2025, **19**, 19777–19789.

4 J. S. Bozich, S. E. Lohse, M. D. Torelli, C. J. Murphy, R. J. Hamers and R. D. Klaper, Surface chemistry, charge and ligand type impact the toxicity of gold nanoparticles to Daphnia magna, *Environ. Sci.: Nano*, 2014, **1**, 260–270.

5 G. Su, H. Zhou, Q. Mu, Y. Zhang, L. Li, P. Jiao, G. Jiang and B. Yan, Effective surface charge density determines the electrostatic attraction between nanoparticles and cells, *J. Phys. Chem. C*, 2012, **116**, 4993–4998.

6 E. McKeel, H. I. Kim, S. J. Jeon, J. P. Giraldo and R. Klaper, The effect of nanoparticle surface charge on freshwater algae growth, reproduction, and lipid production, *Environ. Sci.: Nano*, 2023, 1–10, DOI: 10.1039/d3en00353a.

7 L. G. Diaz and R. Klaper, Phenotypic profiling reveals polystyrene nanoplastics elicit sublethal and lethal effects on cellular morphology in rainbow trout gill epithelial cells, *Environ. Sci.: Nano*, 2025, **12**, 2021–2033.

8 K. Kim, S. J. Jeon, P. Hu, C. M. Anastasia, W. F. Beimers, J. P. Giraldo and J. A. Pedersen, Sulfolipid density dictates the extent of carbon nanodot interaction with chloroplast membranes, *Environ. Sci.: Nano*, 2022, **9**, 2691–2703.

9 S. J. Jeon, P. Hu, K. Kim, C. M. Anastasia, H. I. Kim, C. Castillo, C. B. Ahern, J. A. Pedersen, D. H. Fairbrother and J. P. Giraldo, Electrostatics Control Nanoparticle Interactions with Model and Native Cell Walls of Plants and Algae, *Environ. Sci. Technol.*, 2023, **57**, 19663–19677.

10 A. AvellanJ. Yun, Y. Zhang, E. Spielman-Sun, J. M. Unrine, J. Thieme, J. Li, E. Lombi, G. Bland and G. V. Lowry, Nanoparticle Size and Coating Chemistry Control Foliar Uptake Pathways, Translocation, and Leaf-to-Rhizosphere Transport in Wheat, *ACS Nano*, 2019, **13**, 5291–5305.

11 Y. Zhang, L. Fu, J. Yan, M. Sun, J. P. Giraldo, K. Matyjaszewski, R. D. Tilton and G. V. Lowry, Star Polymer Size, Charge Content, and Hydrophobicity Affect their Leaf Uptake and Translocation in Plants, *Environ. Sci. Technol.*, 2021, **55**, 10758–10768.

12 N. J. Niemuth, D. N. Williams, A. C. Mensch, Yi Cui, G. Orr, Z. Rosenzweig and R. Klaper, Redesign of hydrophobic quantum dots mitigates ligand-dependent toxicity in the nematode C. elegans, *NanoImpact*, 2021, **22**, 100318.

13 B. B. Manshian, D. F. Moyano, N. Corthout, S. Munck, U. Himmelreich, V. M. Rotello and S. J. Soenen, High-content imaging and gene expression analysis to study cell-nanomaterial interactions: The effect of surface hydrophobicity, *Biomaterials*, 2014, **35**, 9941–9950.

14 S. M. Egger, K. R. Hurley, A. Datt, G. Swindlehurst and C. L. Haynes, Ultraporous mesostructured silica nanoparticles, *Chem. Mater.*, 2015, **27**, 3193–3196.

15 T. L. O'Keefe, B. Tuga, C. Deng, S. Mohamud, R. Jamous, M. A. Sanders, W. H. Elmer, J. C. White and C. L. Haynes, Vacuum infiltration for priming of soybean seeds: optimization and particle tracking using fluorescent silica nanoparticles, *Chem. Sci.*, 2025, **16**, 7249–7263.

16 A. L. Lee, B. P. Gee, S. A. Einstein, A. R. Juelfs, H. L. Ring, K. R. Hurley, S. M. Egger, G. Swindlehurst, M. Garwood, W. C. K. Pomerantz and C. L. Haynes, Oxygen Sensing with Perfluorocarbon-Loaded Ultraporous Mesostructured Silica Nanoparticles, *ACS Nano*, 2017, **11**, 5623–5632.

17 J. T. Buchman, W. H. Elmer, C. Ma, K. M. Landy, J. C. White and C. L. Haynes, Chitosan-Coated Mesoporous Silica Nanoparticle Treatment of *Citrullus lanatus* (Watermelon): Enhanced Fungal Disease Suppression and Modulated Expression of Stress-Related Genes, *ACS Sustainable Chem. Eng.*, 2019, **7**, 19649–19659.

18 P. Goswami, J. Mathur and N. Srivastava, Silica nanoparticles as novel sustainable approach for plant growth and crop protection, *Heliyon*, 2022, **8**, 1–12.

19 M. D. Machado and E. V. Soares, Features of the microalga *Raphidocelis subcapitata*: physiology and applications, *Appl. Microbiol. Biotechnol.*, 2024, **108**, 219.

20 A. Riaz, A. Deng, G. Chen, W. Jiang, Q. Zheng, B. Riaz, M. Mak, F. Zeng and Z. H. Chen, Molecular Regulation and Evolution of Redox Homeostasis in Photosynthetic Machinery, *Antioxidants*, 2022, **11**, 1–23.

21 E. Ostovich and R. Klaper, Using a novel multiplexed algal cytological imaging (MACI) assay and machine learning as a way to characterize complex phenotypes in plant-type organisms, *Environ. Sci. Technol.*, 2024, **58**, 4894–4903.
22 E. Ostovich, A. Henke, C. Green and R. Klaper, Predicting the phytotoxic mechanism of action of $LiCoO_2$ nanomaterials using a novel multiplexed algal cytological imaging (MACI) assay and machine learning, *Environ. Sci.: Nano*, 2024, **11**, 507–517.
23 W. G. T. Willats, The cell walls of green algae: a journey through evolution and diversity, *Front. Plant Sci.*, 2012, **3**, 1–7.
24 J. Huebinger, J. Spindler, K. J. Holl and B. Koos, Quantification of protein mobility and associated reshuffling of cytoplasm during chemical fixation, *Sci. Rep.*, 2018, **8**, 17756.
25 D. R. Stirling, M. J. Swain-Bowden, A. M. Lucas, A. E. Carpenter, B. A. Cimini and A. Goodman, CellProfiler 4: improvements in speed, utility and usability, *BMC Bioinf.*, 2021, **22**, 1–11.
26 J. Schindelin, I. Arganda-Carreras, E. Frise, V. Kaynig, M. Longair, T. Pietzsch, S. Preibisch, C. Rueden, S. Saalfeld, B. Schmid, J. Y. Tinevez, D. J. White, V. Hartenstein, K. Eliceiri, P. Tomancak and A. Cardona, Fiji: An open-source platform for biological-image analysis, *Nat. Methods*, 2012, **9**, 676–682.
27 RStudio Team, *RStudio: Integrated Development Environment for R*, 2020.
28 R Core Team, *R: A Language and Environment for Statistical Computing*, 2019.
29 F. Rohart, B. Gautier, A. Singh and K.-A. Lê Cao, mixOmics: An R package for 'omics feature selection and multiple data integration, *PLoS Comput. Biol.*, 2017, **13**, 1–14.
30 J. Bond, L. Donaldson, S. Hill and K. Hitchcock, Safranine fluorescent staining of wood cell walls, *Biotech. Histochem.*, 2008, **83**, 161–171.
31 F. Baldacci-Cresp, C. Spriet, L. Twyffels, A. S. Blervacq, G. Neutelings, M. Baucher and S. Hawkins, A rapid and quantitative safranin-based fluorescent microscopy method to evaluate cell wall lignification, *Plant J.*, 2020, **102**, 1074–1089.
32 OECD, Test No. 201: Freshwater Alga and Cyanobacteria, Growth Inhibition Test, Organization for Economic Cooperation and Development, *OECD Guidelines for Testing of Chemicals, Section 2*, OECD Publishing Service, Paris, France, 2011, pp. 1–25, DOI: 10.1787/9789264069923.
33 P. J. Miller and D. F. Shantz, Covalently functionalized uniform amino-silica nanoparticles. Synthesis and validation of amine group accessibility and stability, *Nanoscale Adv.*, 2020, **2**, 860–868.
34 W. Dou, Y. Niu and X. Liu, Preparation of single-layer antireflective SiO_2 coating with broadband transmittance using PEG-modified sol – gel method, *J. Sol-Gel Sci. Technol.*, 2013, **68**, 302–306.
35 J. S. Suk, Q. Xu, N. Kim and J. Hanes, Ensign PEGylation as a strategy for improving nanoparticle-based drug and gene delivery, *Adv. Drug Delivery Rev.*, 2016, **99**, 28–51.
36 L. Shi, J. Zhang, M. Zhao, S. Tang, X. Cheng, W. Zhang, W. Li, X. Liu, H. Peng and Q. Wang, Effects of polyethylene glycol on the surface of nanoparticles for targeted drug delivery, *Nanoscale*, 2021, **13**, 10748–10764.
37 J. Maillard, K. Klehs, C. Rumble, E. Vauthey, M. Heilemann and A. Fürstenberg, *Chem. Sci.*, 2021, **12**, 1352–1362.
38 A. L. Gonçalves, C. Ferreira, J. A. Loureiro, J. C. M. Pires and M. Simões, Surface physicochemical properties of selected single and mixed cultures of microalgae and cyanobacteria and their relationship with sedimentation kinetics, *Bioresour. Bioprocess.*, 2015, **2**, 1–10.
39 M. A. Nawaz, F. Azeem, A. M. Zakharenko, X. Lin, R. M. Atif, F. S. Baloch, T. F. Chan, G. Chung, J. Ham, S. Sun and K. S. Golokhvast, In-silico exploration of channel type and efflux silicon transporters and silicification proteins in 80 sequenced viridiplantae genomes, *Plants*, 2020, **9**, 1–21.
40 H. Chou, S. Chiu and T. Hu, Quantitative Analysis of Macrophage Uptake and Retention of Fluorescent Organosilica Nanoparticles, *ACS Appl. Nano Mater.*, 2023, **7**, 1–31.
41 K. Blaas and A. Holzinger, F-actin reorganization upon de- and rehydration in the aeroterrestrial green alga *Klebsormidium crenulatum*, *Micron*, 2017, **98**, 34–38.
42 S. Ahrens, S. Zelenay, D. Sancho, P. Hanč, S. Kjær, C. Feest, G. Fletcher, C. Durkin, A. Postigo, M. Skehel, F. Batista, B. Thompson, M. Way, C. Reis e Sousa and O. Schulz, F-Actin Is an Evolutionarily Conserved Damage-Associated Molecular Pattern Recognized by DNGR-1, a Receptor for Dead Cells, *Immunity*, 2012, **35**, 635–645.
43 K. W. Dunn, M. M. Kamocka and J. H. McDonald, A practical guide to evaluating colocalization in biological microscopy, *Am. J. Physiol.*, 2011, **300**, 723–742.
44 J. W. D. Comeau, S. Costantino and P. W. Wiseman, A guide to accurate fluorescence microscopy colocalization measurements, *Biophys. J.*, 2006, **91**, 4611–4622.
45 L. Bashline, S. Li, C. T. Anderson, L. Lei and Y. Gu, The endocytosis of cellulose synthase in arabidopsis is dependent on μ2, a clathrin-mediated endocytosis adaptin, *Plant Physiol.*, 2013, **163**, 150–160.
46 N. Yan and W. X. Wang, Novel Imaging of Silver Nanoparticle Uptake by a Unicellular Alga and Trophic Transfer to *Daphnia magna*, *Environ. Sci. Technol.*, 2021, **55**, 5143–5151.
47 M. R. Krejci, B. Wasserman, L. Finney, I. McNulty, D. Legnini, S. Vogt and J. Derk, Selectivity in biomineralization of barium and strontium, *J. Struct. Biol.*, 2011, **176**, 192–202.
48 F. Li, Y. Hou, L. Chen and Y. Qiu, Advances in silica nanoparticles for agricultural applications and biosynthesis, *Adv. Biotechnol.*, 2025, **3**, 14.
49 A. Pollio, G. Pinto, R. Ligrone and G. Aliotta, Algologia: Effects of the potential allelochemical α-asarone on growth. Physiology and ultrastructure of unicellular green algae, *G. Bot. Ital.*, 1993, **127**, 499.
50 Y. Hong, H. Y. Hu and F. M. Li, Growth and physiological responses of freshwater green alga *Selenastrum capricornutum* to allelochemical ethyl 2-methyl acetoacetate

(EMA) under different initial algal densities, *Pestic. Biochem. Physiol.*, 2008, **90**, 203–212.

51 A. Shebanova, T. Ismagulova, A. Solovchenko, O. Baulina, E. Lobakova, A. Ivanova, A. Moiseenko, K. Shaitan, V. Polshakov, L. Nedbal and O. Gorelova, Versatility of the green microalga cell vacuole function as revealed by analytical transmission electron microscopy, *Protoplasma*, 2017, **254**, 1323–1340.

52 H. Zhang, Y. Ge, X. Xie, A. Atefi, N. K. Wijewardane and S. Thapa, High throughput analysis of leaf chlorophyll content in sorghum using RGB, hyperspectral, and fluorescence imaging and sensor fusion, *Plant Methods*, 2022, **18**, 1–17.

53 T. Jakob, U. Schreiber, V. Kirchesch, U. Langner and C. Wilhelm, Estimation of chlorophyll content and daily primary production of the major algal groups by means of multiwavelength-excitation PAM chlorophyll fluorometry: Performance and methodological limits, *Photosynth. Res.*, 2005, **83**, 343–361.

54 N. Manzoor, L. Ali, T. Ahmed, M. Rizwan, S. Ali, M. S. Shahid, R. Schulin, Y. Liu and G. Wang, Silicon oxide nanoparticles alleviate chromium toxicity in wheat (*Triticum aestivum L.*), *Environ. Pollut.*, 2022, **315**, 120391.

55 T. Yamagishi, H. Yamaguchi, S. Suzuki, Y. Horie and N. Tatarazako, Cell reproductive patterns in the green alga *Pseudokirchneriella subcapitata* (=*Selenastrum capricornutum*) and their variations under exposure to the typical toxicants potassium dichromate and 3,5-DCP, *PLoS One*, 2017, 1–12, DOI: 10.1371/journal.pone.0171259.

56 M. D. Machado and E. V. Soares, Reproductive cycle progression arrest and modification of cell morphology (shape and biovolume) in the alga *Pseudokirchneriella subcapitata* exposed to metolachlor, *Aquat. Toxicol.*, 2020, **222**, 1–9.

57 C. Silva, A. O. Medeiros, A. Converti, F. C. G. Almeida and L. A. Sarubbo, *Biosurfactants: Promising Biomolecules for Agricultural Applications*, 2024.

